

Enhanced stability and superconductivity of IrTe₂/In₂Se₃ heterobilayers with ferroelectrically switchable band topology

Jianyong Chen ^{1,2} Wei Qin,^{1,3} Ping Cui ^{1,4,*} and Zhenyu Zhang ^{1,4,†}

¹*International Center for Quantum Design of Functional Materials (ICQD), Hefei National Research Center for Physical Sciences at Microscale, University of Science and Technology of China, Hefei, Anhui 230026, China*

²*College of Science, Guilin University of Aerospace Technology, Guilin 541004, China*

³*Department of Physics, University of Science and Technology of China, Hefei, Anhui 230026, China*

⁴*Hefei National Laboratory, University of Science and Technology of China, Hefei 230088, China*



(Received 24 May 2023; accepted 13 July 2023; published 4 August 2023)

Recent advances in realizing ferroelectric and superconducting two-dimensional heterobilayers provide appealing platforms for exploring the interplay between ferroelectricity and superconductivity, which is not only crucial for understanding the superconducting mechanism but also important for designing next-generation superconducting devices. Based on first-principles calculations, we demonstrate that an IrTe₂ monolayer can be stabilized on a ferroelectric In₂Se₃ monolayer via interlayer coupling. The superconducting transition temperature of the IrTe₂/In₂Se₃ heterobilayer is substantially enhanced from that of bulk IrTe₂ mainly due to enhanced interlayer coupling, supplemented by the increase in the density of states at the Fermi level and phonon softening; the latter is further tied to Fermi surface nesting. Our calculations show that superconductivity is dominant over several typical competing orders, including charge density wave, magnetism, and nematicity. Moreover, we find that the band topology of IrTe₂/In₂Se₃ can be switched between trivial and nontrivial by reversing the ferroelectric polarization of the In₂Se₃ substrate. By further substituting Ir with Pd, the topological edge states can be tuned close to the Fermi level, making IrTe₂/In₂Se₃ a potential candidate for realizing topological superconductivity. Our work provides a realistic system that can simultaneously harbor ferroelectricity, superconductivity, and nontrivial band topology, paving the way for integrating multiple applications, such as superconducting field transistors, topological quantum computing, and tunable superconducting diodes, in a single system.

DOI: [10.1103/PhysRevB.108.085408](https://doi.org/10.1103/PhysRevB.108.085408)

I. INTRODUCTION

Ferroelectric field control of superconductivity is important for new-type superconducting circuits due to its nonvolatile, bistable, and high spatial precision characteristics [1–3]. Ferroelectric tuning of superconductivity has been achieved in heterostructures made of traditional superconducting and ferroelectric films [4–6]. In contrast to traditional nanostructures that are accompanied with dangling bonds and trap states at the surface, two-dimensional (2D) materials are covalently bonded, with dangling-bond-free atomic layers. The weak van der Waals (vdW) interactions between neighboring layers allow the integration of highly disparate materials [7]. Therefore, a natural strategy to realize ferroelectric tuning of superconductivity in nanoscale is to integrate 2D ferroelectric and superconducting monolayers.

Among the rich library of 2D ferroelectric materials [8], atomically thin In₂Se₃ is unique and more promising for future applications due to its ultrarobust ferroelectricity [9,10] and facile preparations [10–13]. Hence, In₂Se₃ is widely studied for tuning electronic properties [9], magnetism [14,15],

and band topology [16,17]. IrTe₂ is a member of the large family of layered transition metal dichalcogenides. At room temperature, bulk IrTe₂ crystalizes into the 1T phase [18]. Upon cooling, it usually (sometimes not) undergoes a first-order phase transition to different kinds of charge-ordered structures and then becomes superconducting below a critical temperature $T_c \sim 3$ K [18,19]. Recently, the 1T phase of IrTe₂ was reported to be stabilized at the temperature scale of T_c in thick nanosheets [20,21]. The crystal structure and electronic properties of IrTe₂ are found to be sensitive to the interlayer coupling [22,23].

The coupling of superconductor and semiconducting layers not only influences the properties on each side but also brings new physics that is absent on either side. For instance, the T_c of monolayer FeSe [24], supported by a large band gap semiconductor, strontium titanate SrTiO₃, is enhanced by one order of magnitude compared with that of bulk FeSe [25]. In an *s*-wave superconductor/topological insulator heterostructure, the superconductivity proximity effect drives the Dirac surface states into topological superconductivity [26,27]. In contrast to the traditional ferroelectric/superconductor heterostructures, where the tuning of superconductivity is dominated by the modulation of carrier density [4–6], the interlayer couplings in 2D ferroelectric/superconductor heterobilayers may play an important role in tuning the superconductivity. To

* cuipg@ustc.edu.cn

† zhangzy@ustc.edu.cn

understand the interplay between ferroelectricity and superconductivity in 2D heterobilayers, several important issues need to be addressed. First, what is the dominant mechanism of ferroelectric tuning of superconductivity? Secondly, can T_c be effectively tuned by reversing the direction of ferroelectric polarization? Thirdly, in view of the conventional wisdom that ferroelectricity and metallicity are mutually exclusive, can ferroelectricity survive in a 2D monolayer when it couples to a metallic monolayer? In this work, we will address these important issues by taking the IrTe₂/In₂Se₃ heterobilayer as a typical example.

In Ref. [28], we have demonstrated the ferroelectric tuning of superconductivity and band topology in the 2D IrTe₂/In₂Se₃ heterobilayer. The present paper aims to present extended studies of this system and serves as the companion to Ref. [28]. This paper is organized as follows. Section II describes the computational details. Section III presents the energetic properties and enhanced structural stability in the IrTe₂/In₂Se₃ heterobilayer compared with bulk IrTe₂. In Sec. IV, we elucidate the origin of the enhanced superconductivity in the IrTe₂/In₂Se₃ heterobilayer. Due to the strong Fermi surface nesting in IrTe₂/In₂Se₃, we discuss and verify the existence of various competing orders. Section V illustrates tunable band topology in the IrTe₂/In₂Se₃ heterobilayer and the effect of substitutional doping. In addition, the polarization reversal is found to be feasible according to our first-principles calculations. In Sec. VI, we discuss the potential applications for manipulating Majorana zero modes and present our conclusion.

II. COMPUTATIONAL DETAILS

First-principles calculations were mainly performed using the QUANTUM-ESPRESSO materials simulation suite [29]. The Perdew-Burke-Ernzerhof (PBE) of parametrized generalized-gradient approximation (GGA) [30] was used to describe the exchange correlation. Norm-conserving pseudopotentials were adopted to represent the interaction between the ionic cores and valence electrons. The interlayer vdW coupling was treated by the semiempirical correction based on the Grimme's scheme (PBE-D2) [31–33] unless otherwise specified. A plane-wave basis with a 70 Ry energy cut-off was used to represent electronic wave functions. All structures were fully relaxed until the forces were smaller than 1×10^{-5} Ry/a.u. The dynamical matrices and electron-phonon coupling (EPC) were calculated using the density functional perturbation theory (DFPT) [34] in the linear response regime. The dynamical matrix was computed on an $8 \times 8 \times 1$ Monkhorst-Pack (MP) [35] q -point grid. The EPC strengths converge when adopting a $24 \times 24 \times 1$ k -point grid with a Marzari-Vanderbilt [36] smearing of 0.02 Ry unless otherwise specified. The flipping barriers and domain wall motion barriers were calculated by the climbing image nudged elastic band (CINEB) method [37] implemented in the Vienna *ab initio* simulation package (VASP) [38]. The edge Green's functions [39] were obtained by using the maximally localized Wannier functions as implemented in WANNIERTOOLS [41].

The EPC strength (λ) is calculated via the isotropic Eliashberg function $\alpha^2 F(\omega)$ [42]:

$$\lambda = 2 \int_0^\infty d\omega \alpha^2 F(\omega) / \omega = \sum_{\mathbf{q}v} \lambda_{\mathbf{q}v}, \quad (1)$$

$$\alpha^2 F(\omega) = \frac{1}{2\pi N(\varepsilon_F)} \sum_{\mathbf{q}v} \frac{\gamma_{\mathbf{q}v}}{\omega_{\mathbf{q}v}} \delta(\omega - \omega_{\mathbf{q}v}), \quad (2)$$

where $\lambda_{\mathbf{q}v}$ is the branch (v)- and momentum (\mathbf{q})-resolved EPC strength, ε_F is the energy at the Fermi level, $N(\varepsilon_F)$ is the Fermi-level density of states, and $\gamma_{\mathbf{q}v}$ and $\omega_{\mathbf{q}v}$ are the phonon linewidth and frequency of the phonon branch v at the wave vector \mathbf{q} , respectively. The $\gamma_{\mathbf{q}v}$ is defined as

$$\lambda_{\mathbf{q}v} = \frac{2}{\hbar N(\varepsilon_F)} \sum_{\mathbf{k}jj'} |g_{\mathbf{k}+\mathbf{q}j',\mathbf{k}j}^{\mathbf{q}v}|^2 \delta(\varepsilon_{\mathbf{k}j} - \varepsilon_F) \delta(\varepsilon_{\mathbf{k}+\mathbf{q}j'} - \varepsilon_F) / \omega_{\mathbf{q}v}, \quad (3)$$

where $g_{\mathbf{k}+\mathbf{q}j',\mathbf{k}j}^{\mathbf{q}v}$ is the EPC matrix element. The Dirac delta functions arise from energy conservation and reflect the nesting effect on the Fermi surface. The phonon linewidth stems from the Fermi's golden rule, obtained as

$$\gamma_{\mathbf{q}v} = 2\pi \omega_{\mathbf{q}v} \sum_{\mathbf{k}jj'} |g_{\mathbf{k}+\mathbf{q}j',\mathbf{k}j}^{\mathbf{q}v}|^2 \delta(\varepsilon_{\mathbf{k}j} - \varepsilon_F) \delta(\varepsilon_{\mathbf{k}+\mathbf{q}j'} - \varepsilon_F). \quad (4)$$

According to Eqs. (3) and (4), $\lambda_{\mathbf{q}v} = \gamma_{\mathbf{q}v} / [\pi \hbar N(\varepsilon_F) \omega_{\mathbf{q}v}^2]$, and the cumulative EPC is then defined as

$$\lambda(\omega) = 2 \int_0^\omega d\omega' \alpha^2 F(\omega') / \omega'. \quad (5)$$

The T_c is evaluated by the McMillan-Allen-Dynes formula [43,44]:

$$T_c = f_1 f_2 \frac{\omega_{\log}}{1.2} \exp \left[\frac{-1.04(1+\lambda)}{\lambda - \mu^*(1+0.62\lambda)} \right], \quad (6)$$

$$\omega_{\log} = \exp \left[\frac{2}{\lambda} \int_0^{\omega_{\max}} \alpha^2 F(\omega) \frac{\ln(\omega)}{\omega} d\omega \right], \quad (7)$$

where ω_{\log} is the logarithmic average of phonon frequencies; μ^* measures the strength of the screened Coulomb interaction with the common value being in the range of 0.10–0.15 [45]. In Eq. (6), f_1 and f_2 are the strong coupling correction and shape correction, which are given in Ref. [44].

III. STRUCTURES, ENERGETICS, AND STABILITIES OF THE IrTe₂/In₂Se₃ HETEROBILAYER

A. Stacking structures and energetics

To find the most stable stacking configuration for IrTe₂/In₂Se₃, we consider three highly symmetric stacking configurations distinguished by the inner Te atom sitting on the top of the inner In (stacking 1), middle Se (stacking 2), and inner Se (stacking 3) atoms, respectively. The energetic stability of these heterostructures is determined by the formation energy (E_b), defined as $E_b = E(\text{In}_2\text{Se}_3) + E(\text{IrTe}_2) - E(\text{heterobilayer})$, with the terms in the right-hand side representing the total energies of the monolayer In₂Se₃, monolayer IrTe₂, and heterobilayer, respectively. As demonstrated in Table I and Ref. [28], we find that the most energetically favorable stacking configuration is stacking 2 for both directions of the ferroelectric polarization in In₂Se₃.

TABLE I. Formation energies of the IrTe₂/In₂Se₃ bilayers with different stackings for two polarization directions. The unit of the energies is eV.

Formation energy	Stacking 1	Stacking 2	Stacking 3
Downward	0.77	0.91	0.58
Upward	0.69	0.81	0.51

To investigate the relative orientation between the In₂Se₃ and IrTe₂ monolayers in the heterobilayer, we construct the twisted supercells by implementing the coincidence lattice method with the choices of six typical twisting angles, using the primitive hexagonal unit cells. The formation energies of these differently oriented heterobilayers are listed in Table II. It is found that the formation energy of the untwisted heterobilayer is obviously larger than that of the others, indicating that the untwisted heterobilayer is the most stable configuration and has the highest chance to form during growth or transferring process.

B. Enhanced structural stability

Previous work reported that a freestanding IrTe₂ monolayer is dynamically unstable [46]. In contrast, the dynamical stabilities of stacking 2 are confirmed by the absence of imaginary phonon frequencies using both the PBE-D2 and vdW-optB86b schemes (see Fig. 1).

Another common structural distortion in 2D materials is the charge density wave (CDW), which is sensitive to the substrate. For example, a CDW develops in a 1H-NbSe₂ monolayer when it is grown on bilayer graphene or *h*-BN that couples weakly with NbSe₂. However, the CDW is completely suppressed in a 1H-NbSe₂ monolayer grown on Au(111) due to the strong coupling between the overlayer and substrate [47]. Another example is 1H-TaS₂; the CDW emerges when it is grown on bilayer graphene [48], while disappears in 1H-TaS₂/Au(111) [49]. To investigate the tendency of forming a CDW (different from dimerization) in IrTe₂/In₂Se₃, we compare the phonon dispersions of this heterobilayer calculated at different temperatures. Here, the decreasing of the temperature effect is mimicked by reducing electronic smearings, which is widely employed to simulate the CDW-related phenomena [50,51]. As shown in Figs. 1(b)–1(e), the phonon frequency softens very slightly by reducing smearing and no

imaginary frequency appears for both polarizations, indicating the absence of a CDW instability in IrTe₂/In₂Se₃.

To understand the enhanced dynamical stability in IrTe₂/In₂Se₃, we calculate the phonon dispersions of the freestanding IrTe₂ monolayer and graphene-supported IrTe₂ monolayer, as shown in Figs. 1(a) and 2. The optimized lattice constants for a freestanding IrTe₂ monolayer and graphene are 3.85 and 2.46 Å. $\sqrt{3} \times \sqrt{3}$ IrTe₂ matches with $\sqrt{7} \times \sqrt{7}$ graphene with the lattice mismatch being 2.5%. The formation energy between IrTe₂ and graphene is 544/513 meV per unit of IrTe₂ for stacking I/II, and the corresponding interlayer spacing between IrTe₂ and graphene is 3.30 and 3.45 Å. The interaction between IrTe₂ and graphene results in a buckling of graphene less than 0.03 Å, indicating negligibly weak interaction. In sharp contrast, the binding energy and interlayer spacing between IrTe₂ and In₂Se₃ are 910 meV per unit of IrTe₂ and 2.54 Å, respectively, indicating the strong coupling between the two layers. For the dynamical stability, as illustrated in Fig. 1(a), two acoustic branches in freestanding IrTe₂ are imaginary in most of the Brillouin zone with the most negative value around the *M* point. As shown in Fig. 2, there are significant negative phonons of the IrTe₂/graphene heterobilayer, suggesting structural instability. The dynamical instability revealed by our calculations is consistent with experimental observations that an IrTe₂ monolayer grown on bilayer graphene exhibits strong dimerization [22]. In IrTe₂/In₂Se₃, dimerization is suppressed by the interlayer coupling, resulting in an enhanced dynamical stability.

IV. SUPERCONDUCTIVITY

A. Superconductivity and CDW in bulk IrTe₂

We first calculate the EPC and *T_c* of bulk IrTe₂ to benchmark the method employed in the present work. As illustrated in Fig. 3, the total EPC strength (λ) of nondistorted (space group *P*-3*m*1) bulk IrTe₂ is calculated to be 0.76, with the three lowest-lying acoustic branches contributing 66% and the two lowest-lying optical branches also contributing substantially. By choosing the Coulomb pseudopotential μ^* as 0.15–0.10, *T_c* is estimated to be 2.99–4.48 K, which agrees well with experimentally reported values of ~ 3 K [20,21]. In bulk IrTe₂, the interplay between superconductivity and charge orders, such as CDW and dimerization, remains as a controversial issue [21,52–56]. Here, we calculate the λ and *T_c* of the bulk 1/5 charge-ordered IrTe₂ [space group *P*-1

TABLE II. Sizes of the supercells, lattice mismatches, total numbers of atoms within the supercells, interlayer distances, and formation energies of IrTe₂/In₂Se₃ heterobilayers with several typical twisting angles. These results are calculated for the downward ferroelectric polarization in In₂Se₃.

Twist angle	In ₂ Se ₃	IrTe ₂	Strain (%)	Number of atoms	Interlayer distance (Å)	Formation energy (eV/IrTe ₂)
0.00°	1 × 1	1 × 1	6.09	8	2.54	0.91
3.58°	$\sqrt{117} \times \sqrt{117}$	$\sqrt{133} \times \sqrt{133}$	0.14	984	1.58	0.81
10.16°	$2\sqrt{7} \times 2\sqrt{7}$	$\sqrt{31} \times \sqrt{31}$	1.47	233	2.49	0.77
16.10°	$2\sqrt{3} \times 2\sqrt{3}$	$\sqrt{13} \times \sqrt{13}$	2.59	99	2.77	0.67
23.41°	4 × 4	$\sqrt{19} \times \sqrt{19}$	2.01	137	2.80	0.67
30.00°	$\sqrt{3} \times \sqrt{3}$	2 × 2	7.53	27	3.12	0.27
47.48°	$\sqrt{19} \times \sqrt{19}$	$\sqrt{21} \times \sqrt{21}$	1.57	158	2.67	0.74

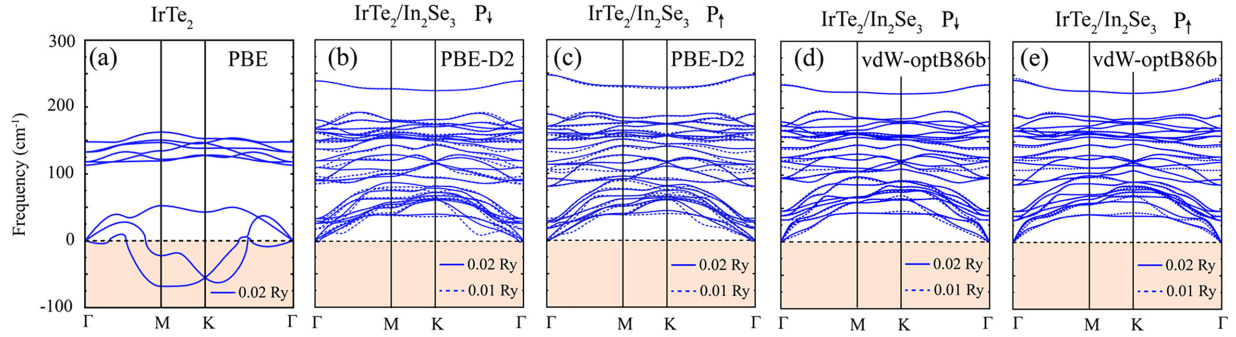


FIG. 1. (a) Phonon spectra of a freestanding monolayer IrTe₂. Phonon spectra of the (b),(d) downward and (c),(e) upward polarized IrTe₂/In₂Se₃ heterobilayers calculated with the (b),(c) PBE-D2 and (d),(e) vdW-optB86b schemes. Solid and dashed blue lines are calculated with smearing of 0.02 and 0.01 Ry, respectively.

(No.2)] [18,55], with the lattice structures and Fermi surfaces shown in Figs. 4(a) and 4(b), respectively. As depicted in the right panel of Fig. 4(c), the total λ is integrated to be ~ 0.40 , resulting in an estimation of $T_c = 0.13\text{--}0.58$ K for $\mu^* = 0.15\text{--}0.10$. The suppression of superconductivity in the P -1 phase of IrTe₂ arises from two aspects. First, the $N(\varepsilon_F)$ of 1/5 charge-ordered IrTe₂ is $\sim 60\%$ of that of nondistorted IrTe₂, as shown in Table III. Secondly, by comparing the real-space distributions of the partial charge within the energy range of -0.05 to 0.05 eV around the Fermi level, we find that the charge of P -3 $m1$ IrTe₂ diffuses between the void space of Ir and Te atoms. However, the Fermi-level charge in 1/5 charge-ordered IrTe₂ is largely localized around the Ir or Te atoms, indicating weaker deformation potential. These calculations show that the formation of typical CDW order in

bulk IrTe₂ weakens superconductivity, supporting the scenario of competition between CDW and superconductivity.

B. Enhanced superconductivity in IrTe₂/In₂Se₃ heterobilayer

We next investigate the superconductivity of the IrTe₂/In₂Se₃ heterobilayer. As reported in Ref. [28] and

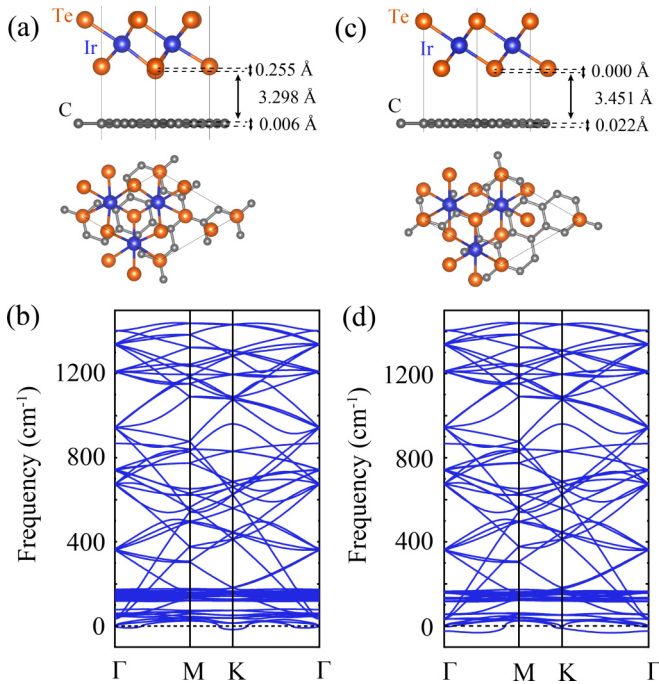


FIG. 2. Phonon dispersions of a $\sqrt{3} \times \sqrt{3}$ IrTe₂/ $\sqrt{7} \times \sqrt{7}$ graphene heterobilayer with stacking configurations (a),(b) I and (c),(d) II, calculated with smearing of 0.02 Ry.

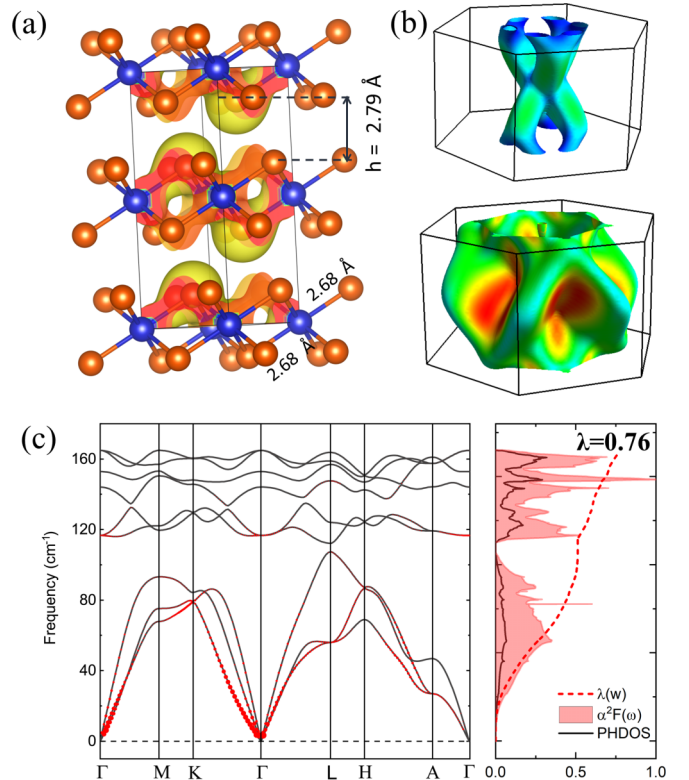


FIG. 3. (a) Optimized crystal structure of bulk IrTe₂ (space group P -3 $m1$) in a $1 \times 1 \times 2$ supercell. The partial charge distribution within the range of -0.05 to 0.05 eV is also depicted. (b) Inner (upper panel) and outer (lower panel) Fermi surfaces. (c) The corresponding phonon spectra with the momentum (\mathbf{q})-resolved EPC strength ($\lambda_{\mathbf{q}}$) indicated by the size of the red circles (left panel). The phonon density of states (PHDOS) (black solid lines), Eliashberg function $\alpha^2F(\omega)$ (pink shaded), and cumulative frequency-dependent EPC strength $\lambda(\omega)$ (red dashed line) are shown in the right panel.

TABLE III. Density of states at the Fermi level $N(\varepsilon_F)$, logarithmic average of the phonon frequencies ω_{\log} , total EPC strength λ , and T_c of bulk IrTe₂ and IrTe₂/In₂Se₃ heterobilayers within the PBE-D2 and vdW-optB86b schemes.

	vdW	$N(\varepsilon_F)$ (Ry ⁻¹)	ω_{\log} (K)	λ	T_c (K) ($\mu^* = 0.15 - 0.10$)
Bulk (SG: $P-3m1$)	PBE-D2	12.27	105.43	0.76	2.99–4.48 ($\sim 3.0^a$)
Bulk (SG: $P-1$)	PBE-D2	7.36	128.49	0.40	0.13–0.58
IrTe ₂ /In ₂ Se ₃ (P_\downarrow)	PBE-D2	20.88	92.33	1.25	7.70–9.58
	vdW-optB86b	21.88	84.23	0.97	4.23–5.58
IrTe ₂ /In ₂ Se ₃ (P_\uparrow)	PBE-D2	19.68	88.53	1.05	5.48–7.14
	vdW-optB86b	19.72	100.34	0.83	3.57–5.08

^aExperimental values [20,21].

summarized in Table III, the T_c 's of the IrTe₂/In₂Se₃ heterobilayers with opposite ferroelectric polarizations are both enhanced compared to the T_c of bulk IrTe₂ ($P-3m1$) (for simplicity, we use ‘‘bulk’’ hereafter). Although the quantitative calculations of T_c depend on a particular vdW correction scheme (vdW-optB86b functional) [57], the result that T_c can be effectively tuned by reversing the ferroelectric polarization direction of In₂Se₃ is robust, as illustrated in Table III and Fig. 5.

By analyzing the density of states, the Fermi surface (FS), phonon dispersion, and EPC strength of bulk IrTe₂ and IrTe₂/In₂Se₃ heterobilayers, we identify the following three important factors related to the T_c enhancement in

IrTe₂/In₂Se₃. (i) Increasing of $N(\varepsilon_F)$: The λ is proportional to the density of states at the Fermi level [58]. As summarized in Table III, the $N(\varepsilon_F)$ of the heterobilayer with either upward or downward polarization is boosted by more than 60% from that of the bulk IrTe₂, indicating significant charge repartitioning around the Fermi level. (ii) Phonon softening: As shown in Fig. 6, the significant change of the atomic environments in the heterobilayers leads to the softening of phonon modes contributed by vibrations of Ir and Te atoms (the EPC is dominated by the IrTe₂ overlayer), resulting in an enhancement of λ according to Eq. (3). (iii) Enhanced FS nesting: The increasing of $N(\varepsilon_F)$ in IrTe₂/In₂Se₃ is also associated with an enhancement of FS nesting, which can be demonstrated from two aspects. First, as shown in Fig. 5(a), all pieces of the Fermi surfaces (except the vertices of the star) in the IrTe₂/In₂Se₃ heterobilayers have parallel partners that are connected (nested) by the wave vectors \mathbf{q}_1 , \mathbf{q}_2 , and their rotations by 60° and 120°. In contrast, the FS nesting in bulk IrTe₂ is much weaker due to the absence of large parallel Fermi surface sheets [see Fig. 3(b)]. Secondly, the $\lambda_{\mathbf{q}\nu}$ of each IrTe₂/In₂Se₃ heterobilayer depends strongly on \mathbf{q} and concentrates in a narrow region around the FS nesting vectors in the Brillouin zone (BZ). This narrow region contributes a large proportion to the total λ . In contrast to the heterobilayer, the $\lambda_{\mathbf{q}\nu}$ of bulk IrTe₂ is uniformly distributed in the BZ except the region close to the Γ point, suggesting the absence of the strong finite- \mathbf{q} FS nesting. Overall, the FS nesting in the IrTe₂/In₂Se₃ heterobilayers is much stronger than that in bulk IrTe₂.

The FS nesting effects on the enhancement of the total λ and branch-resolved λ_ν are not transparent due to the integrations over the phonon wave vectors. An effective approach was developed to calculate the EPC strength by including the phonon softening effect [59]. The total λ can be formally decomposed as [59]

$$\lambda = N(\varepsilon_F) \left(V_0 + \frac{2|M_c|^2}{\omega'^2} \right), \quad (8)$$

where V_0 represents contribution from phonons that are rarely affected by the Kohn anomaly, $|M_c|^2$ denotes an effective coupling matrix element of the relevant phonon modes, and ω' is the renormalized phonon frequency due to the Kohn anomaly. For an acoustic phonon, the renormalized frequency is given by $\omega'^2(\mathbf{q}) = \omega_0^2(\mathbf{q}) - |g_{ep}(\mathbf{q})|^2 \chi_0(\mathbf{q})$ [60], where $\omega_0(\mathbf{q})$ is the bare phonon frequency; $g_{ep}(\mathbf{q})$ and $\chi_0(\mathbf{q})$ are the EPC matrix and particle-hole susceptibility, respectively. Since $\chi_0(\mathbf{q})$ exhibits logarithmically divergent behaviors at the FS nesting

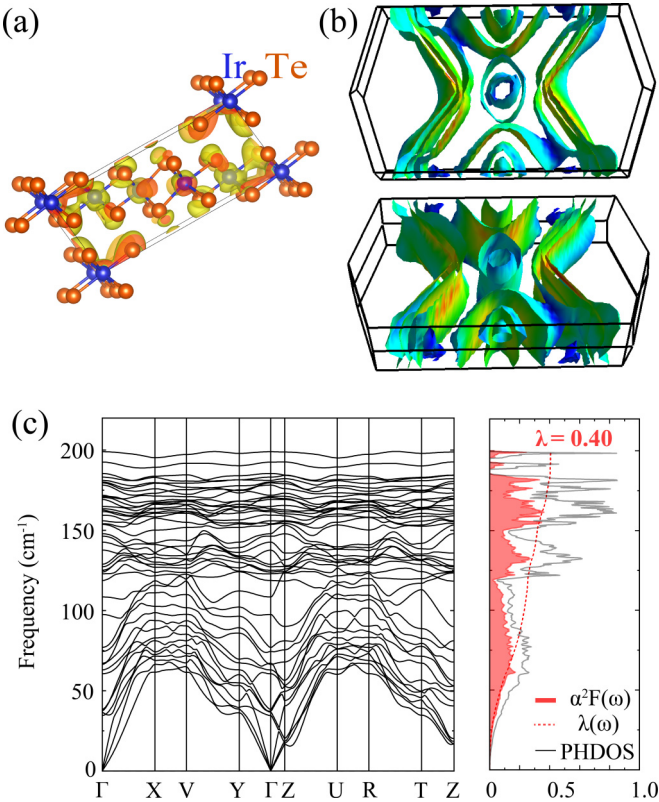


FIG. 4. (a) Optimized crystal structure of bulk 1/5 charge-ordered IrTe₂ [space group $P-1$ (No. 2)] and the partial charge distribution within the range of -0.05 to 0.05 eV. (b) Fermi surfaces. (c) Left panel: Phonon spectra. Right panel: PHDOS (gray solid lines), $\alpha^2 F(\omega)$ (pink shaded), and $\lambda(\omega)$ (red dashed line).

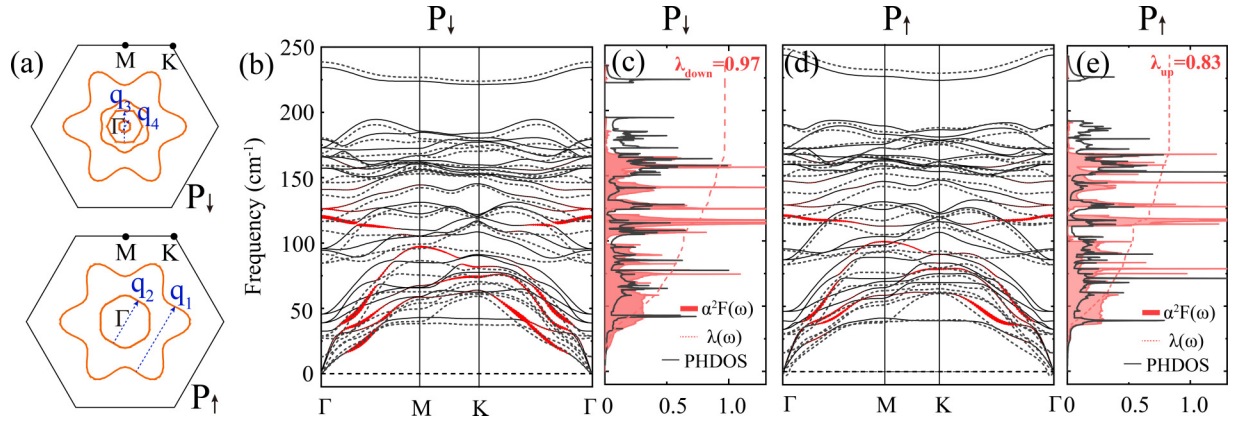


FIG. 5. (a) Fermi surfaces calculated with PBE-D2, with nesting vectors \mathbf{q}_1 , \mathbf{q}_2 , \mathbf{q}_3 , and \mathbf{q}_4 indicated. Phonon spectra, PHDOS, $\alpha^2F(\omega)$, and $\lambda(\omega)$ for the (b),(c) downward and (d),(e) upward polarizations calculated with the vdW-optB86b functional. The phonon spectra calculated with the PBE-D2 scheme are also shown in (b),(d) by the dashed lines for comparison.

wave vectors, the relevant phonon energy will be significantly softened by particle-hole fluctuations [59,61,62], leading to enhancements of the EPC strength [see Eq. (3)] and superconducting transition temperature.

For the heterobilayers with opposite ferroelectric polarization directions, we have $\lambda_{\text{down}}/\lambda_{\text{up}} = 1.19$, which is larger than $N(\varepsilon_F)_{\text{down}}/N(\varepsilon_F)_{\text{up}} = 1.06$ (see Table III), also suggesting that the enhancement of superconductivity in the downward polarization cannot be only attributed to the enhancement of density of states, and that other factors such as phonon softening may play important roles. From Fig. 1(b) in Ref. [28] or Fig. 5, we see that the eight low-frequency phonon branches (branches 1–8 from low to high frequencies) have

been softened for the downward polarization as compared with the upward case. According to Fig. 7, their corresponding contributions to the EPC strengths are 0.93 and 0.74, while the remaining 16 branches collectively contribute an equal EPC strength of 0.30 for both cases. The increasing of $N(\varepsilon_F)$ and weak softening of phonons in the downward polarization can explain the tiny change of the EPC for phonon branches 2–8, but cannot account for branch 1 whose EPC strength in the downward polarization case is two times that of the upward case. It is noted that the deformation potential caused by some specific phonon motion can also be a factor to enhance the EPC strength. Since the phonon branches 2–8 are not sensitive to the interlayer states, the corresponding deformation potentials under different polarizations can be viewed as the same. In contrast, the deformation potential caused by a phonon motion of branch 1 results in an enhancement of $\lambda_{\mathbf{q}_v}$ by a factor of ~ 2.3 when the polarization is switched from upward to downward (see Fig. 2(d) in Ref. [28]), indicating that the pronounced enhancement of λ for branch 1 originates from the enhanced interlayer electron-phonon coupling.

C. Competing orders

Now we discuss potential competing orders in the $\text{IrTe}_2/\text{In}_2\text{Se}_3$ heterobilayer in the presence of FS nesting including particle-particle channel instabilities (non- s -wave superconductivity) and particle-hole channel instabilities (CDW, magnetic, nematicity, etc.). We first recall the explicit definition of two kinds of FS nesting: (i) particle-particle channel FS nesting is characterized by $\varepsilon_{\mathbf{k}+\mathbf{q}} = \varepsilon_{-\mathbf{k}}$; (ii) particle-hole channel FS nesting is characterized by $\varepsilon_{\mathbf{k}+\mathbf{q}} = -\varepsilon_{\mathbf{k}}$, where $\varepsilon_{\mathbf{k}}$ is the electron band energy, and \mathbf{q} denotes the nesting wave vector. For a system with time-reversal symmetry and/or inversion symmetry, the FS is always nested in the $\mathbf{q} = 0$ particle-particle channel due to $\varepsilon_{\mathbf{k}} = \varepsilon_{-\mathbf{k}}$. The FSs shown in Fig. 5(a) are nested by the wave vectors \mathbf{q}_1 , \mathbf{q}_2 , \mathbf{q}_3 , \mathbf{q}_4 in the particle-hole channels.

For pure electronic mechanisms of superconductivity, the particle-hole channel FS nesting plays an important role in driving pairing instabilities in unconventional (non- s -wave) superconductors. A typical example is the

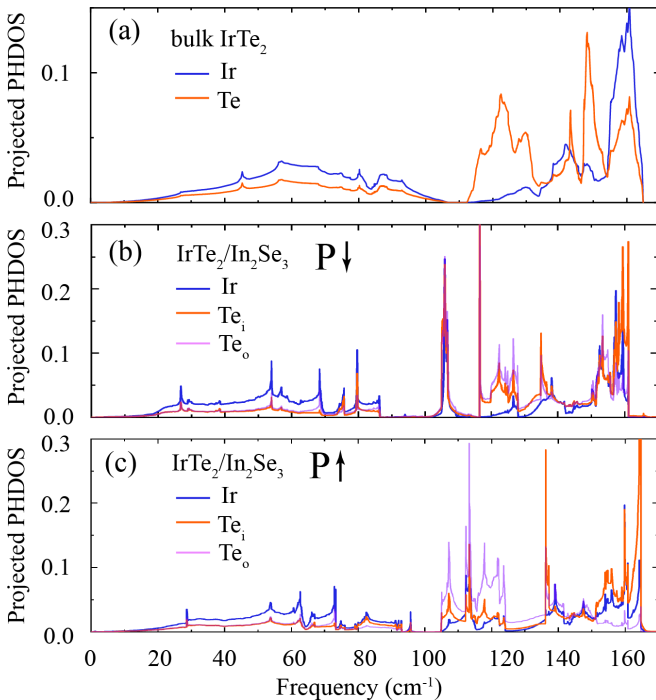


FIG. 6. Atom-projected PHDOS for (a) bulk IrTe_2 ($P\text{-}3m1$) and the $\text{IrTe}_2/\text{In}_2\text{Se}_3$ heterobilayers with (b) downward and (c) upward polarizations.

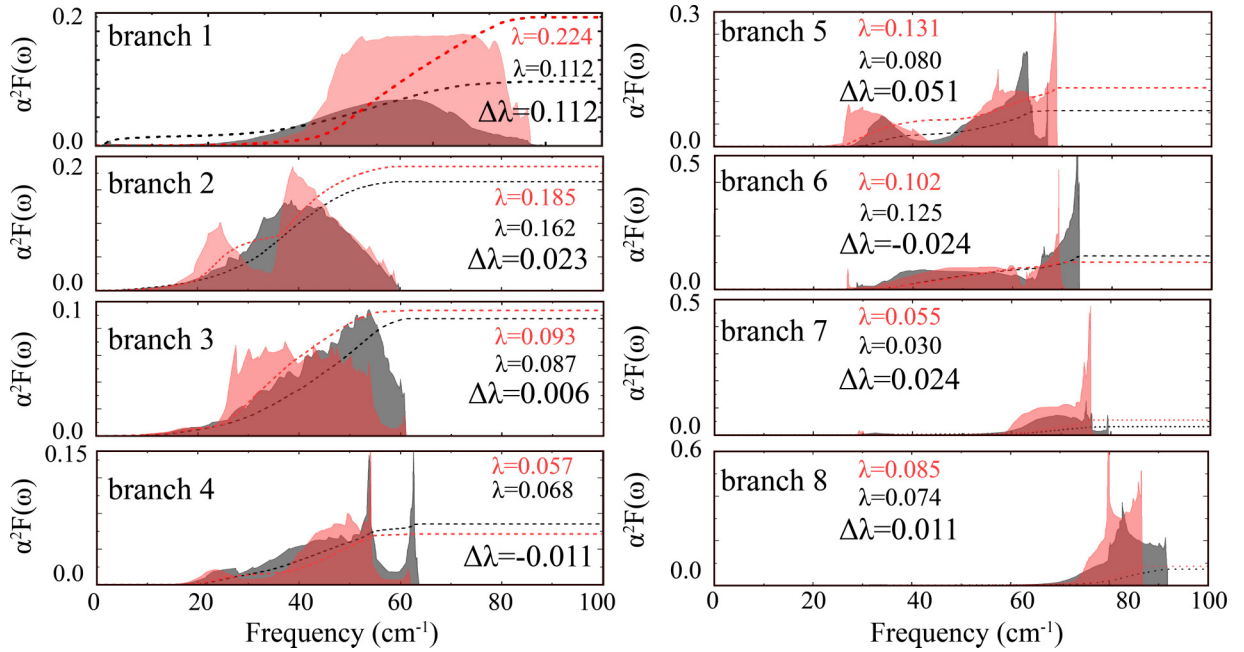


FIG. 7. Branch-resolved $\alpha^2 F(\omega)$ (shaded regions) and cumulative frequency-dependent coupling $\lambda(\omega)$ (dashed lines) for the downward (red) and upward (dark gray) polarizations.

Kohn-Luttinger mechanism of superconductivity [63], where the pairing interaction is obtained by including contributions from second-order particle-hole fluctuations. In particular, the FS crossing ($q = 2k_F$) nesting leads to an anisotropically screened Coulomb interaction that contains attractive components in higher angular momentum channels. Another example is the high- T_c cuprate superconductor, where the $q = (\pi, \pi)$ FS nesting is widely believed to be responsible for the spin density wave (SDW) and zero- q d -wave pairing instabilities [64]. The dominant ordering tendency is determined by the competition between the SDW and d -wave pairing, which in turn is dependent on the degree of FS nesting in the particle-hole channels. For a given system such as the IrTe₂/In₂Se₃ heterobilayers, experimental measurements and/or quantitative theoretical calculations are required to pin down the nature of its superconducting state. For example, if the phonon-mediated attraction overwhelms the Coulomb repulsion in the s -wave channel (which is highly likely to happen in IrTe₂/In₂Se₃ due to the strong EPC strength found in our calculations), a superconducting order with zero q and opposite spin pairings is more likely to be selected, as demonstrated in IrTe₂/In₂Se₃.

Secondly, we investigate the most prominent particle-hole channel instability in IrTe₂-related systems, i.e., CDW. As discussed above, the Kohn anomaly characterized by a dramatic softening of a phonon mode is caused by the FS nesting. In an extreme case, the phonon frequency (commonly associated with an acoustic phonon) may become imaginary upon reducing the temperature, indicating a lattice distortion based CDW instability [50,65,66]. The role of FS nesting in inducing CDW becomes more transparent within a pure electronic mechanism because the corresponding particle-hole channel susceptibility is logarithmically divergent for perfect FS nesting. Equipped by the above concepts, we come back to investigate the potential competing orders in the IrTe₂/In₂Se₃

heterobilayers. One possible candidate order is the finite- q CDW state that was predicted and revealed in earlier studies of bulk and nanoflake IrTe₂ [21,52–55]. In fact, IrTe₂ is likely to be a CDW material with strong electron-phonon coupling [22,67] because the Ir-Ir distance in the dimerized CDW state is strikingly $\sim 20\%$ shorter than that of the nondimerized normal state. This value is much larger than the distortion of 1%–7% in conventional CDW materials [65,68]. Moreover, both theoretical and experimental studies have shown that the structural stability of IrTe₂ is sensitive to the environment [22,69]. Inspired by these earlier studies, we mainly focus on exploring the lattice distortion type CDW instability in IrTe₂/In₂Se₃. Our first-principles calculations show that the softest phonon modes at low temperatures are associated with two types of out of plane vibrations (see α_1 and α_2 in Figs. 1 and 2 in Ref. [28]), which are different from the in-plane imaginary modes appearing in 2D CDW materials such as NbSe₂. Although the freestanding monolayer IrTe₂ exhibits two pronounced imaginary phonon branches, there is no imaginary phonon mode for the IrTe₂/In₂Se₃ heterobilayer, indicating the heterobilayer is dynamically stable against the development of a CDW order (see Fig. 1). This result is valid for both downward and upward ferroelectric polarization directions in the In₂Se₃ substrate.

Finally, we check three typical instabilities based on *ab initio* calculations. (i) Magnetic instabilities: We consider the nonmagnetic, ferromagnetic, Néel antiferromagnetic, stripe antiferromagnetic, and zigzag antiferromagnetic intralayer magnetic configurations in the heterobilayer. The generalized gradient function (GGA)+ U and GGA + U + spin-orbit coupling (SOC) approaches have been employed to approximate the electronic correlation effects, with adjusted on-site repulsion energy U and exchange interaction J (U – J is set to be 0, 1.0, 2.0, and 3.0 eV). After fully relaxing the atomic positions, we find that all the magnetic configurations

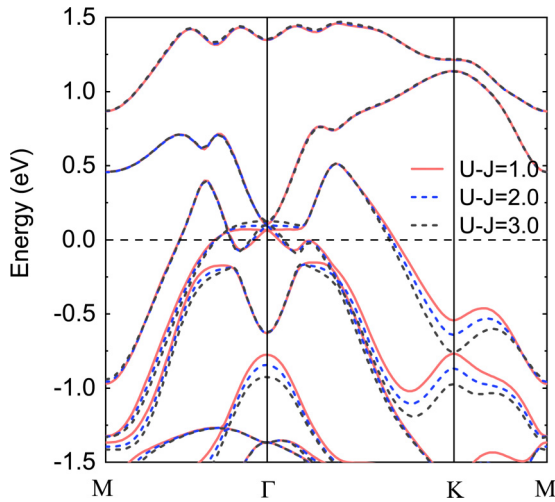


FIG. 8. Band structures of an $\text{IrTe}_2/\text{In}_2\text{Se}_3$ heterobilayer calculated within the $\text{GGA}+U$ method.

converge to the nonmagnetic ground state with identical total energy and vanishing magnetic moment on each atom. These results indicate that $\text{IrTe}_2/\text{In}_2\text{Se}_3$ is unlikely to develop magnetic order. (ii) Metal-insulator transition: As shown in Fig. 8, the band structures near the Fermi level are nearly unchanged after taking into account electronic correlation via the $\text{GGA}+U$ algorithm [70], with $U-J$ being 1.0, 2.0, and 3.0 eV. These results suggest that the metallicity of $\text{IrTe}_2/\text{In}_2\text{Se}_3$ is well preserved. (iii) Nematic instability: The nematic order breaks discrete lattice rotational symmetry while preserving lattice translational symmetry [71]. To search potential nematic phase in $\text{IrTe}_2/\text{In}_2\text{Se}_3$, we generate a set of initial wave functions that break the lattice rotational symmetry, and feed those wave functions to the lattice- and atom-undistorted cell as the starting configuration for subsequent iterative calculations (this method was adopted recently to successfully reproduce the electronic nematicity in FeSe [72]). In our calculations, different initial wave functions are generated from a preparatory converged calculation with $U - J = 3.0$ eV under three different conditions: (a) a randomly distorted atomic cell that slightly breaks the lattice rotational symmetry, (b) a uniaxially strained cell, and (c) an Ir atom shifted along the x or y axis. The symmetrization routine in VASP is turned off for allowing spontaneous electronic symmetry breaking. We find the energy landscape for the final run converges to that of the undistorted cell, and the spatial charge distribution also well respects the space group of the undistorted cell, regardless of the preconditioned distortions. We therefore rule out the nematic instability in the heterobilayer.

Overall, electronic instabilities with different manifestations are usually associated with strong electronic correlations, as reflected by the presence of prominent FS nesting and/or the proximity to van Hove singularity in the density of states. Such characters can be found in our recently explored systems of $\text{Pb}_3\text{Bi}/\text{Ge}(111)$ [73], twisted bilayer graphene [74], and CsV_3Sb_5 [75]. To conclude this section, although there is strong FS nesting in the particle-hole channel, detailed calculations show that the $\text{IrTe}_2/\text{In}_2\text{Se}_3$ heterobilayer is unlikely to harbor particle-hole channel electronic instabilities.

V. TOPOLOGICAL PROPERTIES

A. Tunable band topology in the $\text{IrTe}_2/\text{In}_2\text{Se}_3$ heterobilayer

The band topology of the $\text{IrTe}_2/\text{In}_2\text{Se}_3$ heterobilayer is switchable from trivial to nontrivial as the polarization is reversed from upward to downward, resulting from the cooperative effects of proper band alignments and inherently strong SOC under the scheme of PBE-D2 [28]. To explore the effect of vdW coupling, we recalculate the electronic band structures and topological properties with the vdW-optB86b functional. As shown in Figs. 9(a) and 9(b), the band inversion between the “highest occupied band” and the “lowest unoccupied band” separated by the curved chemical potential [blue dashed line in Fig. 9(b)] occurs for the downward polarization with the SOC, ensuring nontrivial topology [see Figs. 9(c) and 9(d)]. In contrast, the heterobilayer with upward polarization is trivial, as illustrated in Figs. 9(e)–9(h). These results demonstrate that the tunability of band topology is robust in these heterobilayers.

B. Feasibility of polarization switching and its correlation with band topology

The prerequisite for tunable T_c and band topology is the persistence of ferroelectricity in In_2Se_3 after forming the heterobilayers. Here we demonstrate that, although ferroelectric In_2Se_3 makes contact with metallic IrTe_2 , the ferroelectricity is still robust. First, at a mechanistic level, the ferroelectricity is dictated by the out of plane and in-plane polarization locking enforced by the unique intralayer covalent bonding of the In_2Se_3 [9,10]. The unique structurally enforced locking of polarizations provides the out of plane polarization with strong resistance against external perturbations induced by the vdW interfacial coupling. Secondly, because the conducting electrons are confined in the superconducting overlayer (see Fig. 2(a) in Ref. [28]), they couple weakly with the middle Se atoms that are responsible for ferroelectricity, satisfying the “weak coupling principle” proposed by Anderson and Blount for realizing ferroelectric metals [76]. Finally, the electric field induced polarization switching and hysteresis loop in In_2Se_3 have been experimentally demonstrated down to bilayer and monolayer thicknesses, with In_2Se_3 directly supported on conductive substrates (e.g., Au 20 nm/Si wafer or SrRuO_3) [10,11]. First-principles calculations show that the flipping barrier is highly asymmetric, with 0.114 (0.095) eV for reversing downward to upward polarizations and 0.019 (0.015) eV for reversing upward to downward polarizations, using the PBE-D2 (vdW-optB86b) schemes (see Fig. 10); these are slightly higher than 0.07 eV of freestanding monolayer In_2Se_3 . Overall, the reversal of polarization is highly likely to be practically feasible.

To get more insight into the relation between polarization and band topology, we calculate the polarizations (P) and topological invariants (Z_2) of the heterobilayer at selective intermediate states along the kinetic pathway for switching the polarization direction (see Fig. 10). The corresponding band structures are shown in Fig. 11. We reveal a one to one correspondence between the polarization and band topology, which can be qualitatively interpreted as follows. A change in the out of plane ferroelectric polarization (including both the

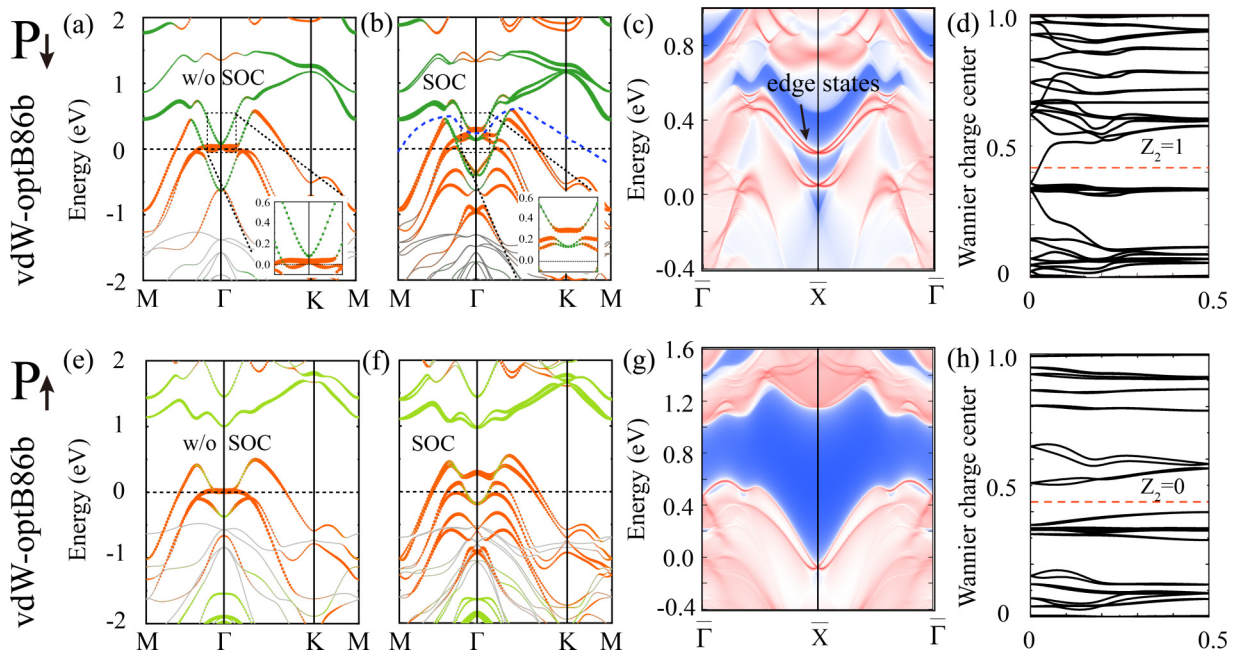


FIG. 9. Band structures for the downward polarization calculated using the vdW-optB86b functional (a) without and (b) with the SOC. The insets are the zoomed-in views. (c) Edge states of the corresponding semi-infinite slab with Te and Se terminations along the zigzag direction, with the $\bar{\Gamma}$ and \bar{X} points in the 1D Brillouin zone of the slab. (d) Evolution of the Wannier charge centers along the k_y direction, with the corresponding topological invariant Z_2 indicated. (e)–(h) Same as (a)–(d) but for the upward polarization. In (a), (b), (e), (f), the sizes of the dark green, light green, and orange circles indicate the contributions from the $\text{In}_o + \text{Se}_o$, $\text{In}_i + \text{Se}_i$, and $\text{Te}-p$ orbitals, respectively.

value and direction) can induce a change in the relative position between the “conduction band” (monotonously shifted to higher energies along the kinetic path) and “valence band” (nearly unchanged) defined by the curved chemical potential, and the band inversion disappears at a specific state of the polarization, causing the transition from the nontrivial to the trivial phase.

In practice, the polarizations are usually flipped by the motion of the domain wall. We also carry out CINEB calculations of the activation barriers for the two common types of domain walls (DW1 and DW2) [9]. As shown in Fig. 12, the barriers are 17.18/6.87 meV/Å² for DW1/DW2 to move left, and 6.87/13.74 meV/Å² for DW1/DW2 to move right. These barrier heights are higher than that of 1.37 meV/Å² for

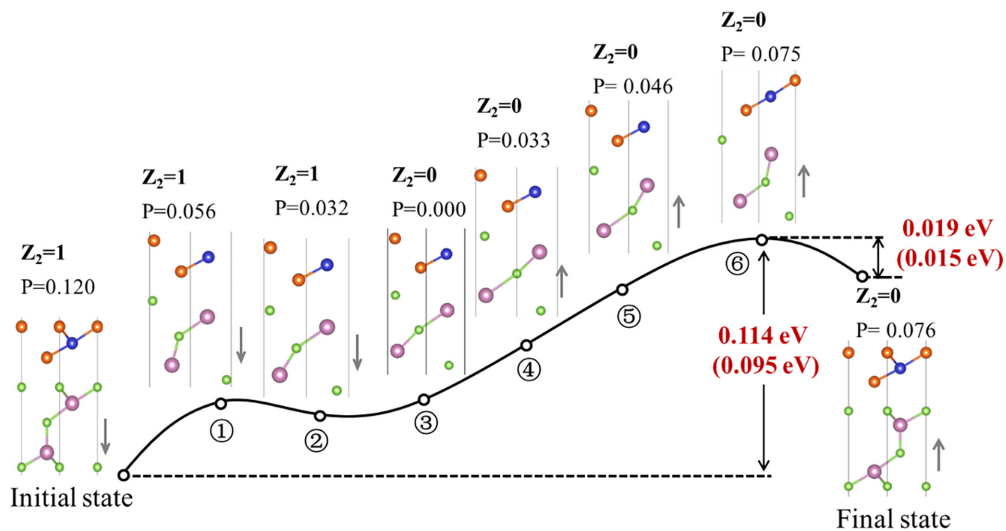


FIG. 10. Kinetic pathway along the trajectory defined by the electric polarization reversal, with six intermediate states (①–⑥) indicated. The flip barriers of 0.114 and 0.095 eV were calculated within the PBE-D2 and vdW-optB86b schemes, respectively. The topological nature (Z_2) and absolute magnitudes of out of plane electric polarizations (P , in units of $e\text{\AA}$) were obtained within the PBE-D2 scheme. The arrows indicate the direction of the net out of plane polarization.

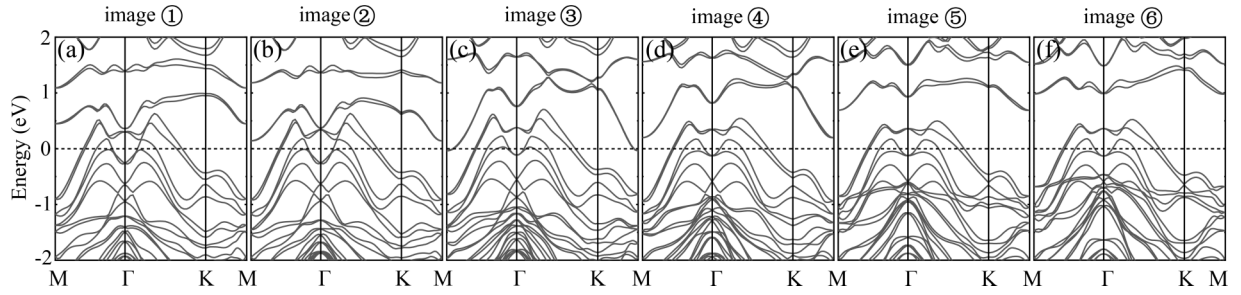


FIG. 11. (a)–(f) Band structures of different intermediate images marked in Fig. 10, calculated with the inclusion of the SOC.

PbTiO₃ [77] and that of $0.36 \text{ meV}/\text{\AA}^2$ for BaTiO₃ [78], but lower than those of 18.55 and $26.79 \text{ meV}/\text{\AA}^2$ for a pristine monolayer In₂Se₃. Qualitatively, lowering of the barriers for the corresponding domain wall motions may be attributed to the weakening of the absolute magnitude of the electric polarization in the heterobilayer. Importantly, since the switching of ferroelectric domains by electric field has been demonstrated experimentally in a pristine monolayer In₂Se₃ [11], we expect that similar controlling manipulation of the ferroelectric domains in IrTe₂/In₂Se₃ can be realized.

C. Tuning the Fermi level by substitutional doping

The coexistence of the topological edge state and the superconducting bulk state within the same energy window is essential for realizing topological superconductivity via reciprocal-space proximity effect [79]. Moreover, the topological edge states have to be close enough to the Fermi level for enabling potential experimental detections [27]. For the IrTe₂/In₂Se₃ heterobilayer, the topological edge states are far above the Fermi level, hindering their effective proximity coupling with the superconducting bulk states to realize topological superconductivity [see Fig. 9(c)].

To move the Fermi level close to the topological edge states, we explore the possibility of electron doping via atomic substitution. Candidate elements are Pd and Pt because they possess identical electronegativity of 2.2 (in units of Pauling scale) to that of Ir. Moreover, the atomic radii of Ir, Pd, and Pt are 136, 138, and 139 pm, respectively, implying small

strain effects of alloying Ir and Pd/Pt. In fact, bulk Ir_{1-x}Pd_xTe₂ [56,80], bulk Ir_{1-x}Pt_xTe₂ [81], and monolayer PdTe₂ [82,83] have already been successfully synthesized. Here we calculate the band structure of Ir_{1-x}Pd_xTe₂ using virtual crystal approximation (VCA) [84,85] for three typical conditions: $x = 0.2$ for Ir-rich condition, $x = 0.5$ for equal doping, and $x = 0.8$ and 1.0 for Pd-rich condition. As confirmed by our Z_2 calculations indicated in Fig. 13, the topological properties of Ir_{1-x}Pd_xTe₂ are robust against doping. By comparing Fig. 13(e) with Fig. 3(c) of Ref. [28], we find that doping Pd into IrTe₂ can effectively shift the Fermi level to higher energy levels, resulting in the intersection with the topological edge states. In addition, electron doping (Pd, Pt) of IrTe₂ suppresses the structural/electronic phase transitions, as demonstrated experimentally in bulk IrTe₂ [56,81].

VI. DISCUSSION AND CONCLUSION

Recently, the proximity effect between topological surface/edge states and superconducting bulk states has been extensively exploited to realize topological superconductivity in realistic material systems [86–91]. To enhance the tunability of the topological superconducting states, external tuning knobs, such as electric gating and charge doping, have been proposed and investigated [92,93]. Compared with these studies, using ferroelectricity as a tuning knob of topological superconductivity proposed in the present work is superior, because ferroelectric tuning is nonvolatile, bistable, and allows for much higher spatial precision in the tunability. The

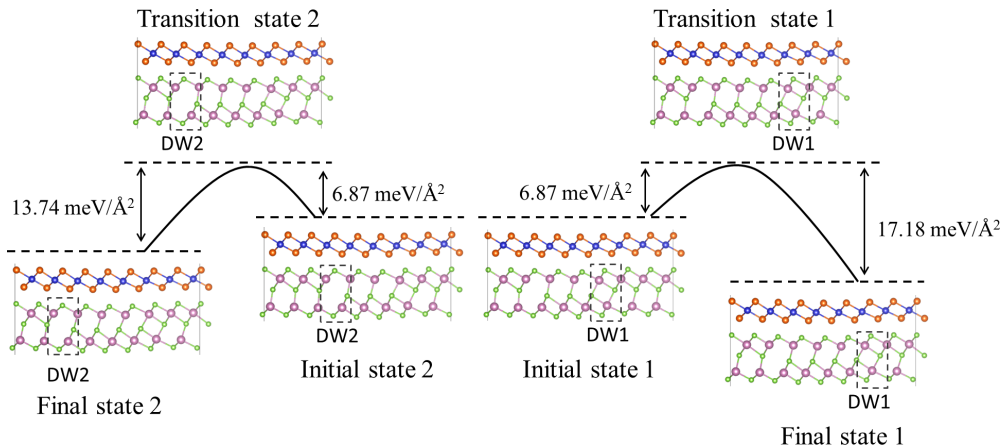


FIG. 12. Minimum energy paths for the domain wall motions in the IrTe₂/In₂Se₃ heterobilayer. The black dashed boxes indicate the locations of the domain walls (DW1 and DW2).

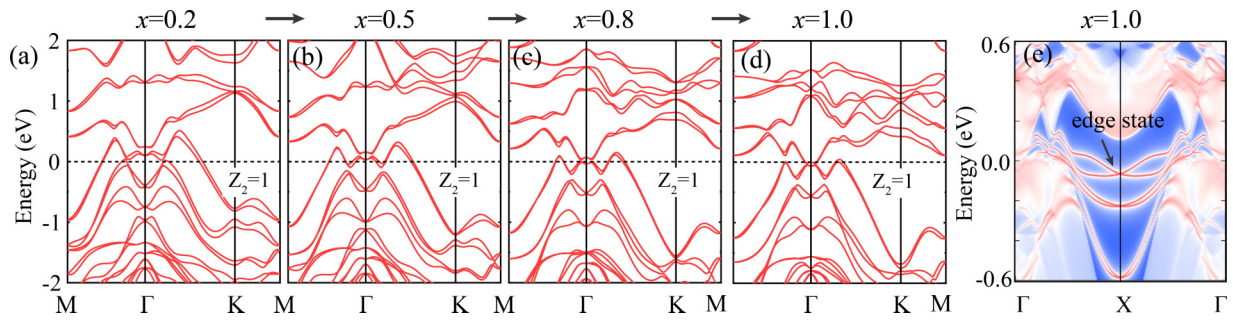


FIG. 13. (a)–(d) Band structures for the downward polarized $\text{Ir}_{1-x}\text{Pd}_x\text{Te}_2/\text{In}_2\text{Se}_3$ calculated with the SOC. (e) Edge states of the $\text{Ir}_{1-x}\text{Pd}_x\text{Te}_2/\text{In}_2\text{Se}_3$ ($x = 1.0$) semi-infinite slab with Te and Se terminations along the zigzag direction of the heterobilayers.

nonvolatile aspect serves as the basis for much faster and low-power tuning, while the bistability can be exploited for more reliable and tunable quantum states. The higher spatial precision in the tunability is inherently tied to the nanoscale ferroelectric domain sizes commonly present in such materials [5], especially in the 2D ferroelectric systems [11]. These merits can be exploited to gain control and manipulation of the topological domains with coexisting superconductivity and resultant topological excitations such as Majorana modes.

In the previous sections, we have shown the coexistence of conventional *s*-wave superconductivity and topologically nontrivial band structure in the $\text{IrTe}_2/\text{In}_2\text{Se}_3$ heterobilayer with downward ferroelectric polarization. By further invoking the proximity effect between the topological edge state and 2D bulk superconducting state [79], it is highly plausible that the edge of the 2D heterostructure hosts quasi-one-dimensional (1D) topological superconducting states, which can be further exploited to harbor Majorana zero modes (MZMs) [26,94]. We envision that, when specified to the $\text{IrTe}_2/\text{In}_2\text{Se}_3$ heterobilayer, MZMs can emerge at the junction between the downward polarized domain and a magnetic insulator [94]. As an optimistic conjecture, here we illustrate in Fig. 14 the creation and manipulation of MZMs (or end modes) that in principle can be created at the boundaries of topologically nontrivial and trivial domains. Yet compared with the earlier studies, the spatial locations of such MZMs can be readily manipulated via the intrinsic ferroelectric polarization, a crucial step, if achieved, in gaining the controlled interaction of multiple MZMs and ultimately their braiding. Given that the latest studies have shown that superconductivity can be tuned by ferroelectricity in a graphene-based heterostructure [95] and a MoTe_2 bilayer [96], it is expected that ferroelectric tuning of the band topology in such systems can be soon achieved as well.

Finally, the spatially separated charge centers in ferroelectric monolayers, combined with the coexistence of inversion symmetry breaking and reversible polarization, should also provide appealing platforms for developing next-generation nanoscale superconducting devices such as reversible field-free superconducting diodes [97] by constructing superconductor/ferroelectric/superconductor vdW heterostructures.

In conclusion, we have demonstrated that the superconducting T_c and band topology of the $\text{IrTe}_2/\text{In}_2\text{Se}_3$ heterobilayer can be simultaneously tuned via changing the ferroelectric polarization direction of In_2Se_3 . Particularly, the

T_c of the heterobilayer is substantially enhanced from that of IrTe_2 nanoflakes, resulting from synergistic effects of enhanced interlayer coupling, the increase in the density of states at the Fermi level, and phonon softening. Due to the uniquely locked ferroelectricity in monolayer In_2Se_3 , and weak coupling between conduction electrons confined in the IrTe_2 overlayer and ferroelectric-related phonon mode in In_2Se_3 , the ferroelectricity survives even when contacting with the metallic overlayer. Moreover, the band topology can be switched from nontrivial to trivial by the reversal of polarizations, and the topology is revealed to be closely related with the direction and magnitude of the polarizations. By substitutional doping of Ir with Pd, the topological edge state can be tuned to the Fermi level, which is essential for realizing potential topological superconductivity. Our work not only provides a realistic platform for realizing simultaneous ferroelectric tuning of superconductivity and band topology but also

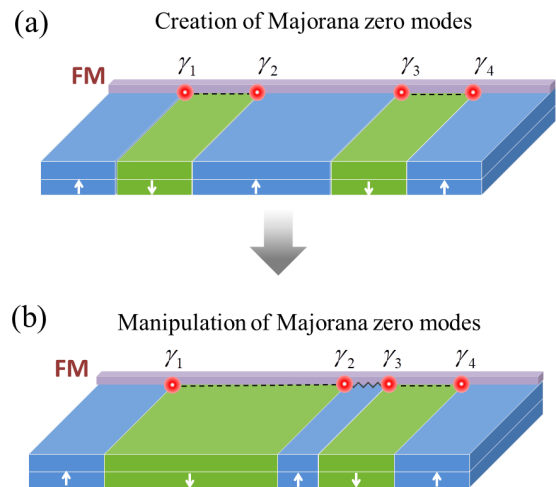


FIG. 14. Schematic diagrams of creating and manipulating MZMs in the $\text{IrTe}_2/\text{In}_2\text{Se}_3$ heterostructure-based platforms. The boundaries between the downward polarization domains (green regions) and a ferromagnetic insulator (lavender region) manifest as 1D topological superconductors due to the proximity effect between 2D bulk superconducting state and 1D Dirac-type topological edge states. (a) Isolated MZMs, where the ferromagnetic insulator can create two MZMs with each downward polarization domain. (b) Manipulation of MZMs by changing the domain size via, for example, externally applied electric field.

uncovers the coupling mechanism of 2D ferroelectric and 2D superconducting monolayers.

ACKNOWLEDGMENTS

We thank Professor Fuchun Zhang for helpful discussions. This work was supported by the Innovation Program for Quantum Science and Technology (Grant No. 2021ZD0302800), the National Natural Science Founda-

tion of China (Grants No. 11974323 and No. 12204121), the National Key R&D Program of China (Grant No. 2017YFA0303500), the Anhui Initiative in Quantum Information Technologies (Grant No. AHY170000), and the Strategic Priority Research Program of the Chinese Academy of Sciences (Grant No. XDB30000000). J.C. also acknowledges the support from the Guangxi Natural Science Foundation (Grants No. 2019GXNSFBA245077 and No. 2021GXNS-FAA220129).

-
- [1] B. Baek, W. H. Rippard, S. P. Benz, S. E. Russek, and P. D. Dresselhaus, *Nat. Commun.* **5**, 3888 (2014).
- [2] V. Fatemi, S. Wu, Y. Cao, L. Bretheau, Q. D. Gibson, K. Watanabe, T. Taniguchi, R. J. Cava, and P. Jarillo-Herrero, *Science* **362**, 926 (2018).
- [3] J. I.-J. Wang, D. Rodan-Legrain, L. Bretheau, D. L. Campbell, B. Kannan, D. Kim, M. Kjaergaard, P. Krantz, G. O. Samach, F. Yan *et al.*, *Nat. Nanotechnol.* **14**, 120 (2019).
- [4] C. H. Ahn, S. Gariglio, P. Paruch, T. Tybell, L. Antognazza, and J. M. Triscone, *Science* **284**, 1152 (1999).
- [5] A. Crassous, R. Bernard, S. Fusil, K. Bouzouane, D. Le Bourdais, S. Enouz-Vedrenne, J. Briatico, M. Bibes, A. Barthélémy, and J. E. Villegas, *Phys. Rev. Lett.* **107**, 247002 (2011).
- [6] K. S. Takahashi, M. Gabay, D. Jaccard, K. Shibuya, T. Ohnishi, M. Lippmaa, and J. M. Triscone, *Nature (London)* **441**, 195 (2006).
- [7] Y. Liu, N. O. Weiss, X. Duan, H.-C. Cheng, Y. Huang, and X. Duan, *Nat. Rev. Mater.* **1**, 16042 (2016).
- [8] Z. Guan, H. Hu, X. Shen, P. Xiang, N. Zhong, J. Chu, and C. Duan, *Adv. Electron. Mater.* **6**, 1900818 (2020).
- [9] W. Ding, J. Zhu, Z. Wang, Y. Gao, D. Xiao, Y. Gu, Z. Zhang, and W. Zhu, *Nat. Commun.* **8**, 14956 (2017).
- [10] J. Xiao, H. Zhu, Y. Wang, W. Feng, Y. Hu, A. Dasgupta, Y. Han, Y. Wang, D. A. Muller, L. W. Martin *et al.*, *Phys. Rev. Lett.* **120**, 227601 (2018).
- [11] F. Xue, W. Hu, K. C. Lee, L. S. Lu, J. Zhang, H. L. Tang, A. Han, W. T. Hsu, S. Tu, and W. H. Chang, *Adv. Funct. Mater.* **28**, 1803738 (2018).
- [12] F. Zhang, Z. Wang, L. Liu, A. Nie, Y. Gong, W. Zhu, and C. Tao, *J. Phys. Chem. Lett.* **12**, 11902 (2021).
- [13] W. Han, X. Zheng, K. Yang, C. S. Tsang, F. Zheng, L. W. Wong, K. H. Lai, T. Yang, Q. Wei, M. Li *et al.*, *Nat. Nanotechnol.* **18**, 55 (2023).
- [14] C. Gong, E. M. Kim, Y. Wang, G. Lee, and X. Zhang, *Nat. Commun.* **10**, 2657 (2019).
- [15] K. Huang, D.-F. Shao, and E. Y. Tsymlal, *Nano Lett.* **22**, 3349 (2022).
- [16] H. Bai, X. Wang, W. Wu, P. He, Z. Xu, S. A. Yang, and Y. Lu, *Phys. Rev. B* **102**, 235403 (2020).
- [17] J.-J. Zhang, D. Zhu, and B. I. Yakobson, *Nano Lett.* **21**, 785 (2021).
- [18] G. Cao, W. Xie, W. A. Phelan, J. F. DiTusa, and R. Jin, *Phys. Rev. B* **95**, 035148 (2017).
- [19] H. Oike, K. Takeda, M. Kamitani, Y. Tokura, and F. Kagawa, *Phys. Rev. Lett.* **127**, 145701 (2021).
- [20] Y. Song, F. Meng, T. Ying, J. Deng, J. Wang, X. Han, Q. Zhang, Y. Huang, J.-g. Guo, and X. Chen, *J. Phys. Chem. Lett.* **12**, 12180 (2021).
- [21] M. Yoshida, K. Kudo, M. Nohara, and Y. Iwasa, *Nano Lett.* **18**, 3113 (2018).
- [22] J. Hwang, K. Kim, C. Zhang, T. Zhu, C. Herbig, S. Kim, B. Kim, Y. Zhong, M. Salah, M. M. El-Desoky *et al.*, *Nat. Commun.* **13**, 906 (2022).
- [23] H. K. Kim, S. Y. Kim, C. J. Won, S.-W. Cheong, J. Kim, J. S. Kim, and T.-H. Kim, *Phys. Rev. B* **107**, 045112 (2023).
- [24] Q.-Y. Wang, Z. Li, W.-H. Zhang, Z.-C. Zhang, J.-S. Zhang, W. Li, H. Ding, Y.-B. Ou, P. Deng, K. Chang *et al.*, *Chin. Phys. Lett.* **29**, 037402 (2012).
- [25] F.-C. Hsu, J.-Y. Luo, K.-W. Yeh, T.-K. Chen, T.-W. Huang, P. M. Wu, Y.-C. Lee, Y.-L. Huang, Y.-Y. Chu, D.-C. Yan *et al.*, *Proc. Natl. Acad. Sci. USA* **105**, 14262 (2008).
- [26] L. Fu and C. L. Kane, *Phys. Rev. Lett.* **100**, 096407 (2008).
- [27] J.-P. Xu, M.-X. Wang, Z. L. Liu, J.-F. Ge, X. Yang, C. Liu, Z. A. Xu, D. Guan, C. L. Gao, D. Qian *et al.*, *Phys. Rev. Lett.* **114**, 017001 (2015).
- [28] J. Chen, W. Qin, P. Cui, and Z. Zhang, companion paper, *Phys. Rev. B* **108**, L060501 (2023).
- [29] P. Giannozzi, S. Baroni, N. Bonini, M. Calandra, R. Car, C. Cavazzoni, D. Ceresoli, G. L. Chiarotti, M. Cococcioni, I. Dabo *et al.*, *J. Phys.: Condens. Matter* **21**, 395502 (2009).
- [30] J. P. Perdew, K. Burke, and M. Ernzerhof, *Phys. Rev. Lett.* **77**, 3865 (1996).
- [31] S. Grimme, J. Antony, S. Ehrlich, and H. Krieg, *J. Chem. Phys.* **132**, 154104 (2010).
- [32] S. Grimme, *J. Comput. Chem* **27**, 1787 (2006).
- [33] V. Barone, M. Casarin, D. Forrer, M. Pavone, M. Sambri, and A. Vittadini, *J. Comput. Chem* **30**, 934 (2009).
- [34] S. Baroni, S. de Gironcoli, A. Dal Corso, and P. Giannozzi, *Rev. Mod. Phys.* **73**, 515 (2001).
- [35] M. Methfessel and A. T. Paxton, *Phys. Rev. B* **40**, 3616 (1989).
- [36] N. Marzari, D. Vanderbilt, A. De Vita, and M. C. Payne, *Phys. Rev. Lett.* **82**, 3296 (1999).
- [37] G. Henkelman, B. P. Uberuaga, and H. Jónsson, *J. Chem. Phys.* **113**, 9901 (2000).
- [38] G. Kresse and J. Furthmüller, *Phys. Rev. B* **54**, 11169 (1996).
- [39] M. P. L. Sancho, J. M. L. Sancho, J. M. L. Sancho, and J. Rubio, *J. Phys. F: Met. Phys.* **15**, 851 (1985).
- [40] A. A. Mostofi, J. R. Yates, Y.-S. Lee, I. Souza, D. Vanderbilt, and N. Marzari, *Comput. Phys. Commun.* **178**, 685 (2008).
- [41] Q. Wu, S. Zhang, H.-F. Song, M. Troyer, and A. A. Soluyanov, *Comput. Phys. Commun.* **224**, 405 (2018).

- [42] G. M. Eliashberg, J. Exptl. Theoret. Phys. (U.S.S.R.) **38**, 966 (1960) [*Sov. Phys. JETP* **11**, 696 (1960)].
- [43] P. B. Allen, *Phys. Rev. B* **6**, 2577 (1972).
- [44] P. B. Allen and R. C. Dynes, *Phys. Rev. B* **12**, 905 (1975).
- [45] J. P. Carbotte, *Rev. Mod. Phys.* **62**, 1027 (1990).
- [46] X. Li, F. Liu, and Q. Wang, *Phys. Rev. B* **102**, 195420 (2020).
- [47] P. Dreher, W. Wan, A. Chikina, M. Bianchi, H. Guo, R. Harsh, S. Mañas-Valero, E. Coronado, A. J. Martínez-Galera, and P. Hofmann, *ACS Nano* **15**, 19430 (2021).
- [48] H. Lin, W. Huang, K. Zhao, C. Lian, W. Duan, X. Chen, and S.-H. Ji, *Nano Res.* **11**, 4722 (2018).
- [49] Y. Yang, S. Fang, V. Fatemi, J. Ruhman, E. Navarro-Moratalla, K. Watanabe, T. Taniguchi, E. Kaxiras, and P. Jarillo-Herrero, *Phys. Rev. B* **98**, 035203 (2018).
- [50] F. Weber, S. Rosenkranz, J. P. Castellán, R. Osborn, R. Hott, R. Heid, K. P. Bohnen, T. Egami, A. H. Said, and D. Reznik, *Phys. Rev. Lett.* **107**, 107403 (2011).
- [51] D. L. Duong, M. Burghard, and J. C. Schön, *Phys. Rev. B* **92**, 245131 (2015).
- [52] S. Park, S. Y. Kim, H. K. Kim, M. J. Kim, T. Kim, H. Kim, G. S. Choi, C. J. Won, S. Kim *et al.*, *Nat. Commun.* **12**, 3157 (2021).
- [53] G. Saleh and S. Artyukhin, *J. Phys. Chem. Lett.* **11**, 2127 (2020).
- [54] H. S. Kim, S. Kim, K. Kim, B. I. Min, Y.-H. Cho, L. Wang, S.-W. Cheong, and H. W. Yeom, *Nano Lett.* **16**, 4260 (2016).
- [55] G.-L. Pascut, K. Haule, M. J. Gutmann, S. A. Barnett, A. Bombardi, S. Artyukhin, T. Birol, D. Vanderbilt, J. J. Yang, S. W. Cheong, and V. Kiryukhin, *Phys. Rev. Lett.* **112**, 086402 (2014).
- [56] J. J. Yang, Y. J. Choi, Y. S. Oh, A. Hogan, Y. Horibe, K. Kim, B. I. Min, and S.-W. Cheong, *Phys. Rev. Lett.* **108**, 116402 (2012).
- [57] J. Klimeš, D. R. Bowler, and A. Michaelides, *Phys. Rev. B* **83**, 195131 (2011).
- [58] G. Profeta, M. Calandra, and F. Mauri, *Nat. Phys.* **8**, 131 (2012).
- [59] S. Blackburn, M. Côté, S. G. Louie, and M. L. Cohen, *Phys. Rev. B* **84**, 104506 (2011).
- [60] C.-J. Kang, K. Kim, and B. I. Min, *Phys. Rev. B* **86**, 054115 (2012).
- [61] G. Profeta, C. Franchini, N. N. Lathiotakis, A. Floris, A. Sanna, M. A. L. Marques, M. Lüders, S. Massidda, E. K. U. Gross, and A. Continenza, *Phys. Rev. Lett.* **96**, 047003 (2006).
- [62] J. Noffsinger, F. Giustino, S. G. Louie, and M. L. Cohen, *Phys. Rev. B* **77**, 180507(R) (2008).
- [63] W. Kohn and J. M. Luttinger, *Phys. Rev. Lett.* **15**, 524 (1965).
- [64] N. Furukawa, T. M. Rice, and M. Salmhofer, *Phys. Rev. Lett.* **81**, 3195 (1998).
- [65] X. Zhu, Y. Cao, J. Zhang, E. W. Plummer, and J. Guo, *Proc. Natl. Acad. Sci. USA* **112**, 2367 (2015).
- [66] R. Bianco, I. Errea, L. Monacelli, M. Calandra, and F. Mauri, *Nano Lett.* **19**, 3098 (2019).
- [67] K. Kim, S. Kim, K. T. Ko, H. Lee, J. H. Park, J. J. Yang, S. W. Cheong, and B. I. Min, *Phys. Rev. Lett.* **114**, 136401 (2015).
- [68] K. Rossnagel, *J. Phys.: Condens. Matter* **23**, 213001 (2011).
- [69] Y. S. Oh, J. J. Yang, Y. Horibe, and S. W. Cheong, *Phys. Rev. Lett.* **110**, 127209 (2013).
- [70] V. I. Anisimov, J. Zaanen, and O. K. Andersen, *Phys. Rev. B* **44**, 943 (1991).
- [71] R. M. Fernandes, A. V. Chubukov, and J. Schmalian, *Nat. Phys.* **10**, 97 (2014).
- [72] X. Long, S. Zhang, F. Wang, and Z. Liu, *npj Quantum Mater.* **5**, 50 (2020).
- [73] W. Qin, L. Li, and Z. Zhang, *Nat. Phys.* **15**, 796 (2019).
- [74] H. Isobe, N. F. Q. Yuan, and L. Fu, *Phys. Rev. X* **8**, 041041 (2018).
- [75] J.-T. Jin, K. Jiang, H. Yao, and Y. Zhou, *Phys. Rev. Lett.* **129**, 167001 (2022).
- [76] P. W. Anderson and E. I. Blount, *Phys. Rev. Lett.* **14**, 217 (1965).
- [77] H.-J. Lee, M. Lee, K. Lee, J. Jo, H. Yang, Y. Kim, C. Chae Seung, U. Waghmare, and H. Lee Jun, *Science* **369**, 1343 (2020).
- [78] X. Y. Li, Q. Yang, J. X. Cao, L. Z. Sun, Q. X. Peng, Y. C. Zhou, and R. X. Zhang, *J. Phys. Chem. C* **122**, 3091 (2018).
- [79] P. Zhang, K. Yaji, T. Hashimoto, Y. Ota, T. Kondo, K. Okazaki, Z. Wang, J. Wen, G. D. Gu, H. Ding *et al.*, *Science* **360**, 182 (2018).
- [80] D. J. Yu, F. Yang, L. Miao, C. Q. Han, M.-Y. Yao, F. Zhu, Y. R. Song, K. F. Zhang, J. F. Ge, X. Yao *et al.*, *Phys. Rev. B* **89**, 100501(R) (2014).
- [81] F. Fei, X. Bo, P. Wang, J. Ying, J. Li, K. Chen, Q. Dai, B. Chen, Z. Sun, and M. Zhang, *Adv. Mater.* **30**, 1801556 (2018).
- [82] C. Liu, C.-S. Lian, M.-H. Liao, Y. Wang, Y. Zhong, C. Ding, W. Li, C.-L. Song, K. He, X.-C. Ma *et al.*, *Phys. Rev. Mater.* **2**, 094001 (2018).
- [83] L. Liu, D. Zemlyanov, and Y. P. Chen, *2D Mater.* **8**, 045033 (2021).
- [84] D. L. Mitchell and R. F. Wallis, *Phys. Rev.* **151**, 581 (1966).
- [85] M. Kriechbaum, K. E. Ambrosch, E. J. Fantner, H. Clemens, and G. Bauer, *Phys. Rev. B* **30**, 3394 (1984).
- [86] J. Gao, W. Ding, S. Zhang, Z. Zhang, and P. Cui, *Nano Lett.* **21**, 7396 (2021).
- [87] G. Bian, T.-R. Chang, A. Huang, Y. Li, H.-T. Jeng, D. J. Singh, R. J. Cava, and W. Xie, *Phys. Rev. Mater.* **1**, 021201(R) (2017).
- [88] Y. Li, Q. Gu, C. Chen, J. Zhang, Q. Liu, X. Hu, J. Liu, Y. Liu, L. Ling, and M. Tian, *Proc. Natl. Acad. Sci. USA* **115**, 9503 (2018).
- [89] Y. Nakajima, R. Hu, K. Kirshenbaum, A. Hughes, P. Syers, X. Wang, K. Wang, R. Wang, S. R. Saha, and D. Pratt, *Sci Adv.* **1**, e1500242 (2015).
- [90] X. L. Peng, Y. Li, X. X. Wu, H. B. Deng, X. Shi, W. H. Fan, M. Li, Y. B. Huang, T. Qian, P. Richard *et al.*, *Phys. Rev. B* **100**, 155134 (2019).
- [91] M. M. Sharma, N. K. Karn, P. Sharma, G. Gurjar, S. Patnaik, and V. P. S. Awana, *Solid State Commun.* **340**, 114531 (2021).
- [92] J.-H. Lee and Y.-W. Son, *Phys. Chem. Chem. Phys.* **23**, 17279 (2021).
- [93] F. Parhizgar and A. M. Black-Schaffer, *Sci. Rep.* **7**, 9817 (2017).
- [94] J. Alicea, *Rep. Prog. Phys.* **75**, 076501 (2012).
- [95] D. R. Klein, L.-Q. Xia, D. MacNeill, K. Watanabe, T. Taniguchi, and P. Jarillo-Herrero, *Nat. Nanotechnol.* **18**, 331 (2023).
- [96] A. Jindal, A. Saha, Z. Li, T. Taniguchi, K. Watanabe, J. C. Hone, T. Birol, R. M. Fernandes, C. R. Dean, A. N. Pasupathy *et al.*, *Nature (London)* **613**, 48 (2023).
- [97] H. Wu, Y. Wang, Y. Xu, P. K. Sivakumar, C. Pasco, U. Filippozzi, S. S. P. Parkin, Y.-J. Zeng, T. McQueen, and M. N. Ali, *Nature (London)* **604**, 653 (2022).